Thin Solid Films 787 (2023) 140120

Contents lists available at ScienceDirect

Thin Solid Films

journal homepage: www.elsevier.com/locate/tsf

In-situ/operando characterization of FeO_x-based chemiresistive sensor of acetone vapours by X-ray absorption spectroscopy

Ján Ivančo [a,*], Simone Pollastri [b], Monika Hofbauerová [a,c]

[a] Institute of Physics, Slovak Academy of Sciences, 84511 Bratislava, Slovakia
[b] ELETTRA Sincrotrone Trieste, 34149 Basovizza (TS), Italy
[c] Centre for Advanced Materials Application, Slovak Academy of Sciences, 84511 Bratislava, Slovakia

ARTICLE INFO

Keywords:
Chemi-resistors
Gas sensor
Acetone sensor
Iron oxide
Nanoparticle film
X-ray absorption spectroscopy
Extended x-ray absorption fine structure
X-ray absorption near edge structure

ABSTRACT

Metal oxide thin films are archetypal active elements employed in chemiresistive gas sensors. Most existing metal oxide-based sensors operate at elevated temperatures; however, the sensing mechanism has generally been deduced considering the room-temperature properties of metal oxide compounds. We report an in-operando X-ray absorption spectroscopy study on a chemiresistive sensor of acetone vapours; namely, the chemical structure of iron-oxide nanoparticles (NPs) exposed to trace concentrations of acetone vapours under varying temperature conditions was examined. Our results show that the iron-oxide NPs, identified as maghemite/magnetite (γ-Fe_2O_3/Fe_3O_4) compound, partially reduced with temperature. Likewise, the iron oxide NPs were partially reduced upon exposure to trace concentrations of acetone vapour (at constant temperature). The latter observation suggests that acetone molecules are chemically adsorbed on iron oxide. The chemical changes are discussed in terms of the conductive response of a consubstantial chemiresistive sensor. Acetone chemisorption requires a revision of the commonly accepted sensing mechanism based on the physical adsorption of acetone molecules.

1. Introduction

Environmental protection requires the detection of trace concentrations of environmentally hazardous gases, such as NO, NO_2, CO, CO_2, SO_2, and Cl_2, including volatile organic compounds (VOCs) present in trace concentrations under ambient conditions. Regarding the detection of VOCs, a more advanced potential would likely shape human medicine; more than 1000 VOCs ranging from ppm- (parts-per-million, 10^{-6}) down to ppb (parts-per-billion, 10^{-9}) and less have been detected in the exhaled breath of a human, with dozens of them already identified as markers for specific diseases [1]. Detecting gaseous or vaporous markers in a patient's exhaled breath would facilitate non-invasive examination [2]. The abovementioned application areas would particularly benefit from the availability of simple sensors that could allow, for instance, areal monitoring of environmentally hazardous gases or provide affordable personal equipment for immediate health screening by detecting VOCs.

The chemiresistive effect, which refers to the conductivity changes of a probe responding to ambient concentration variations, provides a viable sensing technique [3]. Typically, semiconducting metal oxides such as FeO_x [4–7], SnO_2 [8], TiO_2 [9], In_2O_3 [10,11], WO_3 [12,13], WO_3-Cr_2O_3 [14], NiO [15], ZnO [16], and others (see Refs. [17,18] and references therein) were used as the active elements in chemiresistive sensors. The sensitivities of such devices vary depending on the nature of the chemiresistive materials and the gaseous or vaporous analytes, with sensitivities even in the low ppb range being reported in particular cases (for example, Refs. [10,12]).

Sensors for detecting trace concentrations of acetone vapours diluted in the air have been widely studied (for example, Refs. [4,5,7,9,12–14,19]), as monitoring acetone concentration in the exhaled breath of patients with diabetes could indicate their current health status. Specifically, the acetone concentration of a healthy person is approximately 0.7 ppmv, and values exceeding about 1.7 ppmv diagnose a diabetic patient [1,20]. These values establish the minimum requirements for the operational detection range of acetone sensors to cover a range from a few hundred parts per billion to approximately 10 ppm.

Unlike early gas sensors based on bulk samples or continuous layers, current approaches rely on nanostructured sensing layers in which the nature of the material, structure, and morphology allow numerous combinations, which led to ample investigations of sensing properties,

* Corresponding author.
E-mail address: jan.ivanco@savba.sk (J. Ivančo).

https://doi.org/10.1016/j.tsf.2023.140120
Received 28 April 2023; Received in revised form 4 October 2023; Accepted 3 November 2023
Available online 4 November 2023

as attested by abundant studies on the subject. However, most studies are limited to a phenomenological description of the sensing properties, while some works adhere to a widely used model of the sensing mechanism of chemiresistors based on the field effect; the conductivity change is related to the variation of the charge-depleted or -enriched region near the semiconductor surface caused by the physisorption of a molecular analyte.

Nevertheless, the modulation of the surface potential may not explicitly result from the semiconducting nature of the material. Indeed, a typical situation is the Fermi-level pinning at the surface, avoiding the field effect control. In addition, the depletion zone width in the nanostructured films could significantly exceed grain size and, accordingly, was inconsistent with the model. Further, the sensing mechanism is usually justified considering the properties of metal-oxide compounds determined at room temperature (RT). Yet, the metal oxide-based sensors show practically no response at RT and require elevated operating temperatures of up to several hundred degrees Celsius (see, for example, Refs. [4–9,11–17,19]). Thus, examining material properties under operating conditions provides a more appropriate view.

This study aimed to test the notion that the chemiresistive response of a typical semiconducting metal-oxide is due to the altered chemistry of the sensing material caused by the adsorbed analyte. The X-ray absorption spectroscopy (XAS), which is widely used for determining the local structure of particular atomic species of matter, was chosen as the primary technique as the probing can be carried out in ambient (hence not requiring vacuum conditions) and at elevated temperatures (e.g. [21,22]). Here, the chemical composition of iron oxide compounds was examined under the operating conditions of a chemiresistive sensor, that is, at elevated temperatures and upon acetone vapour exposure. The results are discussed in the context of the electrical response of the sensor based on the identical active element.

2. Experimental

2.1. The probed samples preparation

Iron oxide nanoparticles (NPs) were synthesized by the thermal decomposition of iron(III) acetylacetonate and subsequently reduced with 1,2-hexadecanediol in a mixture of oleic acid and oleylamine, which was used as the surfactant precursor in phenyl ether at elevated temperatures. The average diameter of the FeO_x NPs was approximately 6.9 nm, including a surfactant thickness of about 1 nm. The preparation of NPs was detailed elsewhere [23].

The probed films were prepared using the modified Langmuir-Schaefer method [24]: an ordered monolayer array of colloid iron oxide NPs deposited onto the water surface was transferred to a solid surface. The process was repeated according to the number of required layers and led to an ordered NP mono- or multilayer (see, e.g. Ref. [25]). Then, the NP films were annealed in a technical vacuum ($p \approx 1.4 \times 10^{-4}$ Pa) at 350 °C for one hour to strip the nanoparticles of the surfactant.

Two samples were prepared to tailor requirements for the characterization techniques:

The XAS sample is a multilayer consisting of ten ordered monolayers of FeO_x nanoparticles sequentially deposited layer-by-layer onto a silicon substrate with a size of 10 × 10 mm and a thickness of 0.6 mm.

The sample for chemiresistive characterization stands out for two nanoparticle monolayers sequentially deposited onto an alumina chip with a size of 2 × 2 mm soldered in a commercial socket. The chip was equipped with Ti/Pt heating meander on the rear side and the Ti/Pt interdigitated electrodes on the front side to examine the resistance. More details can be found elsewhere [26].

2.2. X-ray absorption spectroscopy characterization

The sample for the XAS measurements was fixed on a ceramic heating plate with temperature monitored by a thermocouple and placed into the probe cell, equipped with feed lines for gas inlet/outlet. First, a constant flow of 10 sccm of dry air was set, and the temperature was stepwise increased to a maximum value of 360 °C. At each step, X-ray absorption near edge structure (XANES) spectra, referred to as 'air', were collected after the sample temperature stabilization. At the highest temperatures used (300, 330, and 360 °C), the 'air' measurement was followed by a measurement upon acetone exposure, referred to as 'acetone': the flow of dry air was replaced by the same flow (10 sccm) of a calibrated mixture of 50 ppm acetone vapours diluted in dry air (SIAD S.p.A., Italy). The 'acetone' measurement was followed by the 'air' measurement at a higher temperature.

Fe K-edge XAS spectra were collected at the XAFS beamline of the ELETTRA synchrotron (Trieste, Italy) [27] in the fluorescence mode using a silicon drift detector with an 80 mm^2 active area (AXAS-M, Ketek, Munich, Germany). The ring current and energy were 300 mA and 2.0 GeV, respectively. A fixed exit Si(111) double-crystal monochromator was used, ensuring high-order harmonic rejection by detuning the second crystal. The monochromator energy was calibrated by collecting a reference spectrum of a Fe metal foil placed in a second experimental chamber after the sample and after the I1 ionization chamber, with the position of the first inflection point taken at 7112.0 eV. Spectra were collected with a variable energy step as a function of energy: A large step (5 eV) in the first 200 eV of the spectrum, a smaller step (0.2 eV) in the XANES region and a *k*-constant step of 0.03 $Å^{-1}$ in the EXAFS region. Each measurement cycle lasted about 6 h.

For each state of the sample (temperature and exposure to air or acetone), four spectra were collected and merged to increase the signal-to-noise ratio, then normalised with respect to the atomic background of the curve using the Athena software [28]. The normalized XANES spectra were then analysed through linear combination fitting (LCF) [21,22,29,30] using reference spectra from maghemite (γ-Fe_2O_3, labelled as MAGH) and magnetite (Fe_3O_4, labelled as MAGN) certified standards compounds (Sigma Aldrich, CAS 1309-37-1 and 1317-61-9, respectively) in the form of pressed pellets, containing the element of interest mixed with polyvinylpyrrolidone binder and collected at room temperature. LCF analysis was performed at least three times on each spectrum, trying different normalization strategies for raw and smoothed data to test the reproducibility of the obtained results; the fitting range was -30–+160 eV with respect to the absorption edge.

The described method of multilayer growth ensures that the 2- and 10-ML thick films have the same morphology (ordered arrays) and chemistry (FeO_x). Therefore, the results obtained by distinct methods are commensurable.

2.3. The sensing response

The sensing response was identified with the ratio R_{acet}/R_{air}, where R_{air} and R_{acet} are the electrical resistivity between the interdigital electrodes examined in dry air and acetone-in-dry air mixture, respectively. The resistivity was standardly investigated at a constant operating voltage of 10 V using a Keithley 2635B SYSTEM Source meter. The acetone concentration in the probing cell was varied by mixing dry air and a certified mixture of 20 ppm acetone vapours diluted in dry air (SIAD, Slovakia). The ratio was controlled by employing mass-flow controllers. The total airflow of 10 sccm was kept constant for each used acetone concentration, including the reference airflow without acetone.

3. Results

3.1. The measured XANES

Fig. 1a shows the normalized Fe K-edge XANES spectra of the series annealed in air. The edges are detailed in Fig. 1b. The detection depth of XAS at the energies around the K absorption edge of Fe significantly exceeds the thickness of the probed layer.

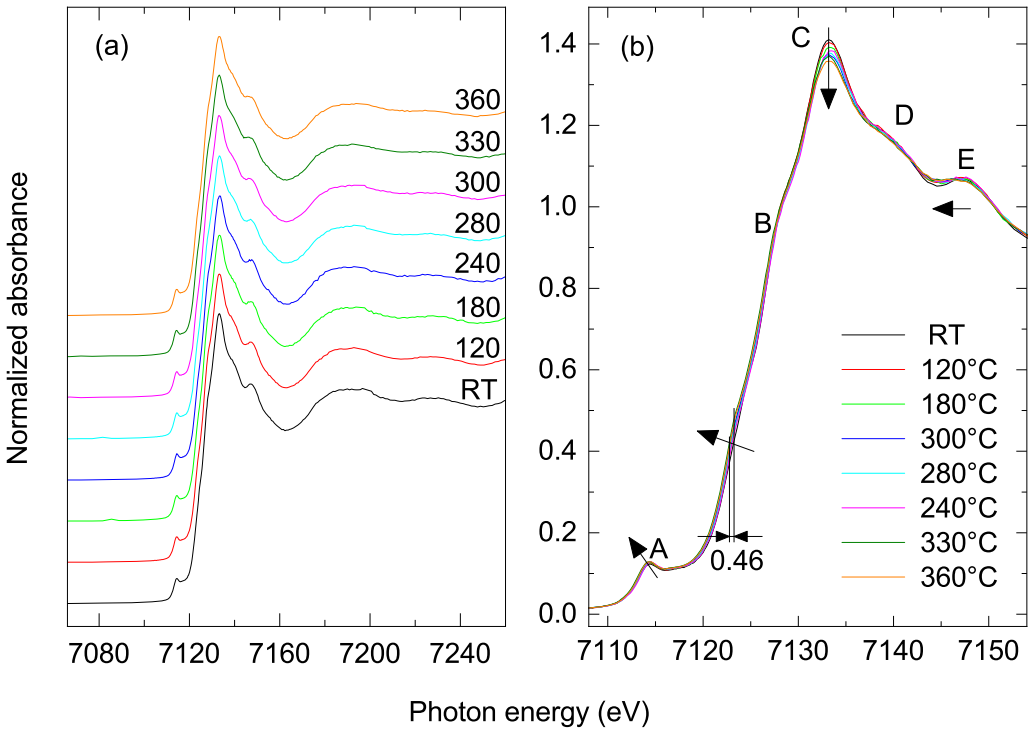

Fig. 1. (a) Fe K-edge XANES spectra of iron-oxide nanoparticle multilayer taken at various temperatures in synthetic air flow. The spectra are vertically shifted. (b) Details of Fe K-edge XANES spectra shown in the panel *a*. Characters A to E refer to the features discussed in the text. The arrows indicate the trends in the spectra evolution with increasing temperature (see the text).

The Fe K-edge region routinely serves to determine particular iron oxide compounds. Therefore, we analysed the line profiles of the following spectral features: the pre-edge peak area (A in Fig. 1b), absorption edge (B), the crest of the absorption edge, also referred to as the white light line (C), and post-edge features (D and E). Pre-edge features of various Fe-based bulk minerals were extensively studied, e.g. by Wilke et al. [31] and Pollastri et al. [32]. In concrete, MAGH, in comparison to MAGN, displays an overall blue shift (toward higher energies) equal to 2–2.5 eV at the half height of the absorption edge [31,33,34].

Regarding the white line intensity, contradictory results have been reported in the literature: Fig. 8a in Ref. [31] highlights the higher intensity of the white line for MAGH, but on the contrary, Fig. 1 in Ref. [33] reports an opposite result. Because the difference between these two phases is small, the relative intensity of the white line could also be influenced by the chosen normalization strategy. However, our spectra collected using certified standards are in line with those reported in [31].

In Fig. 1b, the arrows next to the corresponding features indicate their evolution with increasing temperature. The edge profile slightly deviates from linearity, indicating that MAGH and MAGN phases coexist. γ-Fe_2O_3 maghemite is a metastable phase with a cubic crystal structure closely related to the Fe_3O_4 magnetite structure.

Considering the findings reported in Refs. [31,33,34], the observed trends of the pre-edge features (A), edge position (B) and post-edge features (E) suggest a partial MAGH → MAGN transition. Considering the issues mentioned above and contradictions in the relative intensities of the white line between MAGH and MAGN, it is difficult to assess whether its evolution (C) in our data set agrees with the MAGH → MAGN transition. However, we assume that arguments rising from the energy scale (features A, B and E) are more appropriate for phase identification.

The presence of haematite (α-Fe_2O_3) seems unlikely here since the features specific to haematite – namely, the weakened pre-edge intensity (blue-shifted with respect to MAGN [35]) and a hump on the low-energy side of the crest (tending to double the white line peak) [31,34,36] – are absent here. It should be, however, mentioned that haematite with an edge free of a hump near the white peak has also been reported [37]. Further, since haematite contains only the 6-fold coordinated Fe being a centrosymmetric position, the pre-edge peak has low intensity (See the inset of Fig. 2a).

The temperature dependence of the white line of the 'air' spectra may suggest the thermal effect [38], but the observed trend is perfectly in line with the energy shift observed for the absorption edge, for which the most reasonable explanation is being a partial transition to a more reduced phase (i.e. magnetite). Therefore, the contribution of the thermal effect in the 'air' spectra cannot be excluded. Yet, the thermal effect is not responsible for the differences in spectra collected in acetone versus those gathered in the air at the same temperature.

For the sake of completeness, we add that attempts to analyse the EXAFS region were also performed but did not provide conclusive evidence, most likely due to the complexity of the fit; note that two phases always coexist, which both contain either tetrahedrally and octahedrally coordinated Fe with similar Fe-O bond lengths (and also Fe^{2+} and Fe^{3+} in the case of magnetite) rising the number of uncertainties to be calculated.

The mixing ratio, the relative content of MAGH and MAGN in the sample, was determined using the LCF of XANES spectra for MAGH and MAGN reference samples. All spectra were treated in an identical way, whereby Fig. 2 illustrates an example of LCF analysis of spectra collected in the air at RT. Because the self-absorption effect is relevant for thicknesses exceeding approximately 1 μm [33], no corrections by virtue of self-adsorption were necessary because the thickness of the probed NPs multilayer was about 70 nm. The overall results are shown in Fig. 3 and indicate that the partial MAGH → MAGN transition occurs in dry air with increasing temperature; the initial maghemite fraction of 77% decreased to 62.3% at 360 °C. The magnetite fraction evolved in a complementary manner, rising from 23 to 37.7%.

The evolution of the mixing ratio in the presented sample indicates a reductive reaction with increasing temperature; MAGH (γ-Fe_2O_3) gradually transforms to MAGN ($Fe_3O_4 = Fe_2O_3 \cdot FeO$) (Fig. 3, full symbols). The reductive reaction with the increased temperature is

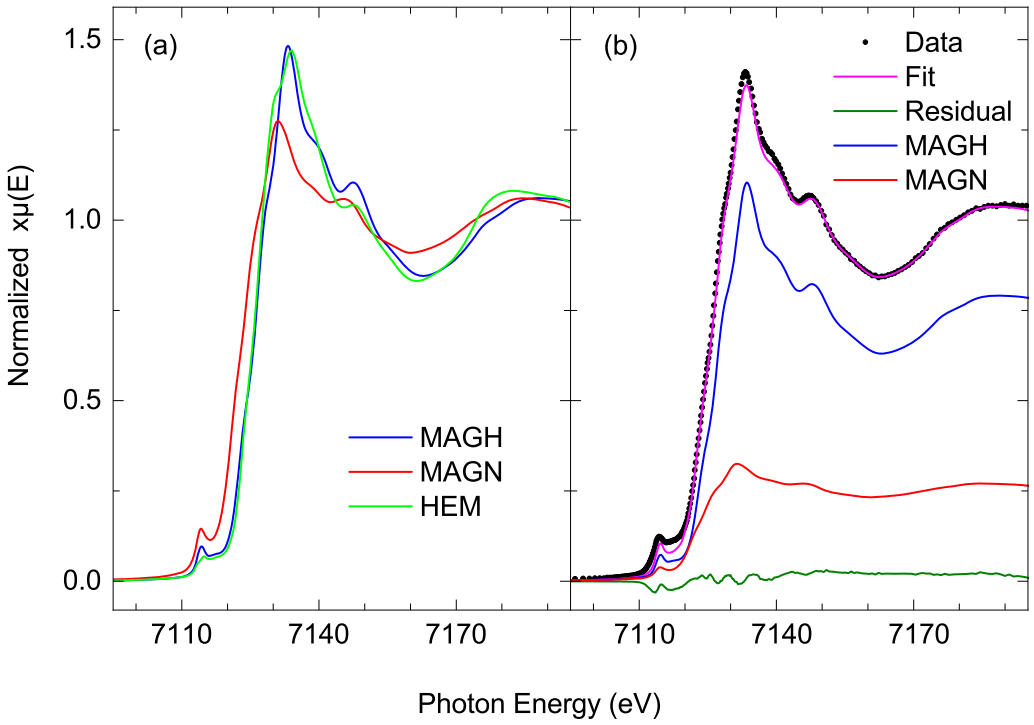

Fig. 2. (a) The reference spectra of maghemite (MAGH, γ-Fe_2O_3), magnetite (MAGN, Fe_3O_4), and haematite (HEM, α-Fe_2O_3) used for the LCF. (b) An example of Linear Combination Fit (LCF) obtained for the RT spectrum collected in air. Only the edge region is shown here.

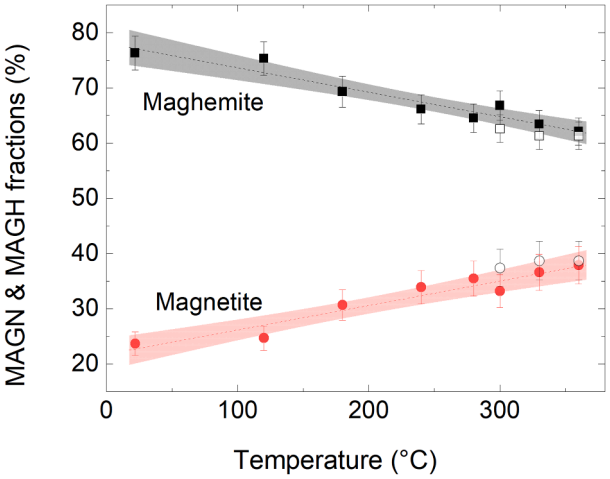

Fig. 3. Evolution of magnetite and maghemite fractions in iron oxide nanoparticles at increasing temperatures in dry air (full symbols) and upon exposure to 50 ppm acetone diluted in dry air (empty symbols). Fractions were determined using the Linear Combination Fit of the reference absorption spectra of γ-Fe_2O_3 (maghemite) and Fe_3O_4 (magnetite). The 95% confidence bands are also presented.

predictable considering the phase diagram for the Fe-O_2 system (see Fig. 2 in Ref. [39]); admittedly, the reduction occurs at relatively lower temperatures, from approximately 200 °C. Yet, it should be noted that the stability of thin nanostructured films under particular conditions depends on many parameters, and the marked departure from the bulk oxide phase diagram can be applied [40,41].

The effect of the acetone exposure was measured at three temperatures, namely at 300, 330, and 360 °C (Fig. 3, empty symbols); the decrease in the MAGH/MAGN mixing ratio at the given temperatures indicates the reductive character of the acetone-induced reaction. Note that the 'acetone' measurement followed after the 'air' measurement at the given temperatures. This may suggest that the reduction upon the acetone exposure is due to the longer exposure of FeO_x at a particular temperature. However, the temperature effect can be excluded in the 'acetone' measurements, considering that each measurement was launched after the sample temperature stabilization. Specifically, the sample temperature stabilized in ca 10 min after the temperature increase of 30 °C. This claim emerged from chemiresistive characterizations, where the electrical resistance stabilized within ca 10 min after the same temperature increase. Moreover, the period necessary for the temperature stabilization was negligible compared to the cycle measurement, lasting ca 6 h. The acetone-induced chemistry is discussed below.

3.2. Sensing properties of the probed NPs layer

Fig. 4a illustrates the chemiresistive response of a FeO film consisting of two arrayed nanoparticle monolayers (ML) to acetone vapours exposure. The film resistance R_{air} measured in dry air drops upon adding acetone with a concentration of 2 ppmv. The R_{acet} refers to maximal resistance departure after the 15 min exposure. The resistance gradually returns to the original value R_{air} after removing the acetone from the mixture. The right axis shows the resistance normalized with respect to R_{air}. The cycle was measured at the film temperature of 402 °C.

Fig. 4b sums R_{air}`s and $R_{acet}$`s of the cycles measured at various temperatures ranging from ca 200 to 460 °C: the R_{air} (circles) and R_{acet} (cross symbols) monotonously decrease with temperature. The markedly lower electrical resistivity of Fe_3O_4 [42] compared to Fe_2O_3 [43] would suggest that the observed resistivity drop is due to the partial transformation of MAGH to MAGN. Yet the reduction is owing to the semiconducting nature of MAGH and MAGN: this results from Arrhenius's plot $\ln(1/R) \propto 1/T$ (Fig. 5) of the data presented in Fig. 4b. The linear dependences strongly indicate the band-like conductivity, though two regions with different activation energies, separated at a temperature of about 430 ℃, are apparent.

The sensor response, i.e. the R_{acet}/R_{air} ratio, is plotted in the inset of Fig. 4b in dependence on temperature. The highest response is at ~ 410

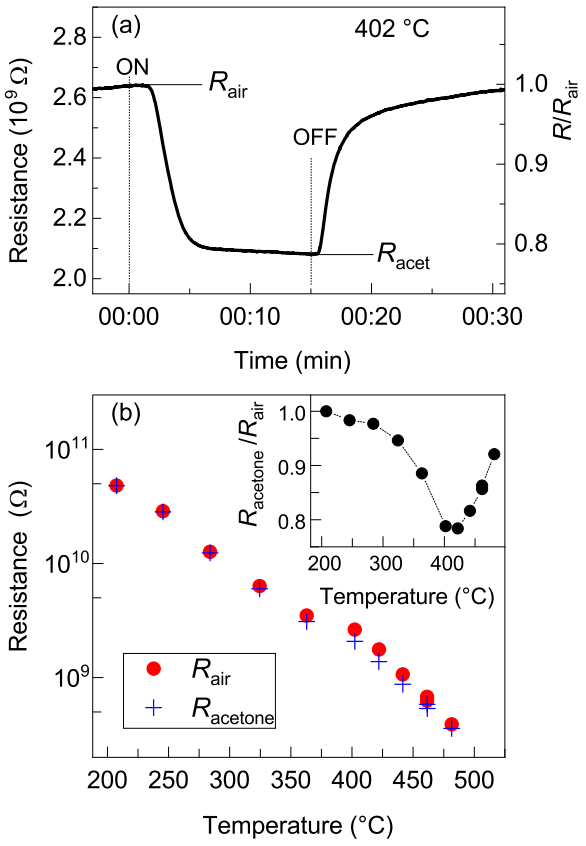

Fig. 4. The response of the layer formed by 2 ML of iron oxide nanoparticles arrays to 2 ppm acetone-in-air mixture. (a) The example of the time dependence of the resistance measured at 402 °C. R_{air} and R_{acet} indicate the resistance in the air and the acetone-in-air mixture, respectively, used to calculated the response. The ON/OFF indicate the points of adding/stopping acetone in the air flow. The delayed responses are due to the period necessary to replace the gas mixture in the probing chamber. (b) R_{air} (full circles) and R_{acet} (+); each couple of values were determined in a particular cycle measured at a set temperature. The inset shows the temperature dependencies of response, that is, the R_{acet}/R_{air} ratio.

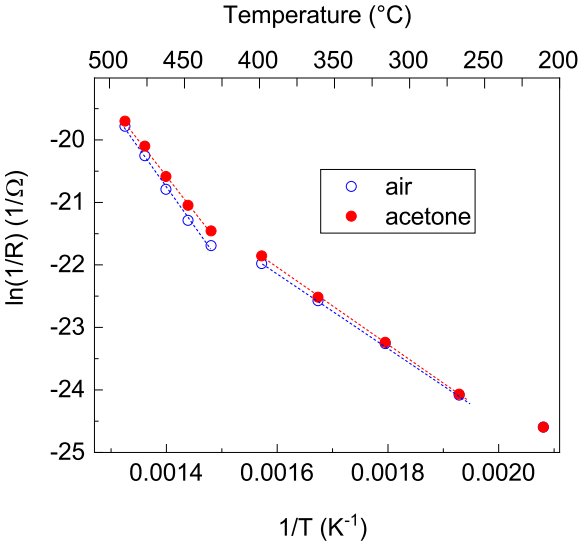

Fig. 5. Arrhenius plots of data shown in Fig.4b. The straight lines are guides to the eye.

°C.

The responses to higher acetone concentrations (6, 10, 14, and 20 ppm were also examined (not shown here). They were qualitatively similar to that at 2 ppm, whilst the R_{acet}/R_{air} ratio (approximately of 0.78, see Fig. 4a and the inset in Fig. 4b) decreased – hence the sensing response increased – down to about 0.2 detected for the 20 ppm acetone exposure. In a convention often observed, the response in which the resistance decreases upon analyte exposure (detected here) is called *n*-type. In contrast, the increase in resistance implies a response with a *p*-type character. Note that the *n*- and *p*-type response of chemiresistive sensors must not be confused with the semiconductor conductivity type.

We mention in passing that the sample probed by XAS consisted of ten monolayers and was exposed to 50 ppm acetone. The higher values compared to those used for the probe examined by electrical characterization were necessitated by the lower sensitivity of the XAS technique compared to the electrical characterization.

4. Discussion

The phase transformation of iron oxide has been extensively studied owing to its extensive technological applications. Numerous studies on the phase transformations induced by thermal treatment have examined probed structures *after* thermal treatment at RT. However, some chemical and structural transformations in iron oxides caused by elevated temperatures can reverse upon returning to RT [40]; this suggests that considerations of the sensing mechanism must accrue from properties responsive to the working temperature of the sensor.

It is reasonable to presume that the oxidizing states at the nanoparticle surface and bulk can differ, and the acetone adsorption effect can be limited to the surface region of the nanoparticles. Considering that the XAS probing depth markedly exceeded the NPs size, the detected signal averaged over the entire nanoparticle volume. Given that the chemical structure of the surface region of NPs differs from that of the bulk, and this may mainly hold upon acetone exposure, the real variations in the chemistry of the NP surface owing to both the elevated temperature and acetone exposure are likely more pronounced compared to the detected ones.

Various surface studies – thence performed under vacuum conditions – addressed reaction pathways of acetone molecules adsorbed on several metal oxide surfaces, such as α-Fe_2O_3 [44], ZnO(0001) [45], TiO_2(001) [46], UO_2(111) [47], and CeO_x(111) [48]. Regarding the acetone adsorption onto haematite [44], two products were formed on the surface at low temperatures, both prone to desorption. However, at elevated temperatures exceeding 250 °C, a new species, acetate ions ($C_2H_3O_2^-$), was formed through either an oxidation mechanism or the involvement of surface hydroxy groups. Overall, other named studies demonstrated that reduced surfaces (alternatively attained through the formation of oxygen surface vacancies or metal atom termination of the crystal surface) lead to reactive adsorption, contrary to the weak or molecular adsorption observed on fully oxidized surfaces. The reactive pathways on the reduced surfaces led to acetone decomposition, prevailingly outputting the CO and CO_2 species.

The aforementioned findings suggest that the acetone molecules adsorb chemically on the partially reduced iron oxide occurring at elevated temperatures. This implies that the surface chemistry change has to be considered when formulating the sensing mechanism.

We expect that the reduction pathway of the MAGH/MAGN compound upon acetone exposure occurs similarly to the acetone/CeO_2(111) system [48]) as follows:

$$CH_3COCH_3(g)+2O(l)\rightarrow 3CO(g)+3H_2(g)+2V_O \quad (1)$$

where V_O denotes oxygen vacancy, and the indices *l* and *g* in parentheses state for the lattice position and the gas phase, respectively, for the particular compound or element.

The O(*l*) consumed by the reaction with acetone presumably derives

from the MAGH component, and its removal transforms MAGH component to MAGN as follows:

$$3Fe_2O_3 = 2[Fe_2O_3 \cdot FeO] + O \quad (2)$$

where Fe_2O_3 and $Fe_2O_3 \cdot FeO = Fe_3O_4$ are MAGH and MAGN, respectively. A decrease in the MAGH component leads to a decrease in the MAGH:MAGN ratio, according to the reduction of the probed iron oxide compound.

The response of metal oxide-based chemiresistive sensors to acetone has been almost exclusively reported to display the peaked temperature dependence, where the highest response occurs at elevated temperatures ranging from about 150 to 500 °C (see an example in the inset of Fig. 4b and Refs. [4–9,11–13,15–17,19]). The physical adsorption of detected molecules is generally considered to rationalize the conductive response of metal oxide-based chemiresistors. Yet, the concentration of physically adsorbed molecular analyte on the sensor surface decreases with temperature (at constant analyte concentration in ambient). Hence the assumption on physical adsorption is at variance with the common observation of negligible sensor response at RT, and its maximal response peaked at hundreds of degrees centigrade. On the other hand, if the acetone chemisorption is assumed, the peaked response can be qualitatively explained considering two surface phenomena following opposing temperature dependences: (*i*) the decrease of the acetone surface coverage and (*ii*) the increasing reaction rate governed by the activation energy.

The metal oxide-based sensors exhibit the peaked temperature dependence of the response also for other vaporous or gaseous analytes; we mention several examples such as nitrogen dioxide (NO_2) [4,7] carbon monoxide (CO) [11], ethanol (C_2H_6O) [5,6,9,16], isopropanol (C_3H_8O) [8], toluene (C_7H_8) [15], and formaldehyde (CH_2O or HCHO) [6], HCN [9], H_2S [9,11]. Therefore, the chemisorption of volatile analytes triggered at elevated temperatures can be a general phenomenon related to metal-oxide-based sensors.

The conductivity of continuous films is governed by Ohm's law. In contrast, the electrical conductance of discontinuous films, for example, those consisting of an array of isolated nanoparticles, is determined by the Ohmic conductance of nanoparticles themselves and the tunnelling current mechanism governing the interparticle conductivity [49,50]. The latter applies because the charge carriers tunnel through the potential barrier formed between two neighbouring, yet isolated nanoparticles separated by a gap. The tunnelling process is relevant for angstrom- or nanometer-sized gaps only when tunnelling current I decays exponentially with the width of the tunnelling gap z:

$$I \propto a e^{-\sqrt{\varphi} z} \quad (3)$$

where constant a and work function φ represent the properties of a particular conducting material. Note that the tunnelling conductivity of the nanoparticle film depends – in addition to the interparticle distance – on the nanoparticles` work function. The term a reflects the NPs resistance varying with the temperature due to the semiconducting character of the iron oxide (Fig. 5).

We note that the dominance of the tunnelling mechanism in nanostructured chemiresistive sensors is also supported by functioning nanostructured strain sensors that employ an array of conductive isolated nanoparticles deposited on a flexible substrate. Neglecting the resistance of conductive nanoparticles, the conductivity of the array depends exponentially on the substrate elongation and, thus, on the interparticle distance (see, for example, Refs. [51,52]).

The α, φ, and z in Eq. (3) are constant at a given temperature, and the sensing response comes from the Δφ induced by the adsorption of the acetone molecule. Therefore, the sensing mechanism is governed by tunnelling conductance varying with the change of the nanoparticle surface work function, not by the conductivity of the nanoparticle.

Wei et al. [53] found that work function values of maghemite (γ-Fe_2O_3) and magnetite (Fe_3O_4) films at RT amount to 5.35 and 5.2 eV, respectively. Assuming that the inequality $\varphi_{Fe3O4} < \varphi_{Fe2O3}$ is preserved at elevated temperatures, MAGH → MAGN transformation induced by acetone adsorption decreases the work function and, thus, increases the film conductivity. In brief, the decrease in the nanoparticle`s work function caused by modified surface chemistry can plausibly explain the *n*-type response characterized by the inequality $R_{acet}/R_{air} < 1$. Note that the *n*-type response excludes the formation of a depletion zone near the surface of the iron oxide nanoparticles owing to acetone adsorption because the presence of the depletion zone would be manifested through the resistance increase.

Responses of various metal oxide-based chemiresistive sensors to volatile adsorbents have similar temperature dependence, inviting speculation that the sensing mechanism of this class of sensors is too governed by the chemisorption. However, further work is necessary to prove the validity of this point.

5. Summary

The chemical structure of the iron-oxide nanoparticles was studied at elevated temperatures and upon exposure to trace concentrations of acetone vapours using Fe K-edge X-ray absorption spectroscopy. We observed that a partial reduction of iron oxide nanoparticles, constituted by maghemite/magnetite compound, was induced by elevated temperature and acetone exposure. Furthermore, the transformation of maghemite to magnetite upon acetone exposure implies that exposure to even trace concentrations of acetone vapour modifies the surface chemistry of the iron oxide nanoparticles. Based on the obtained results, a revision of the standard model of the sensing mechanism is proposed.

Funding

Support for this research was provided by the CERIC funding scheme (Proposal No. 20177056); Scientific Grant Agency VEGA (Project No. 2/0142/23); Slovak Research and Development Agency (Project No. APVV-14-0891).

CRediT authorship contribution statement

Ján Ivančo: Conceptualization, Formal analysis, Funding acquisition, Investigation, Methodology, Project administration, Writing – original draft, Writing – review & editing. **Simone Pollastri:** Data curation, Formal analysis, Investigation, Validation, Writing – review & editing. **Monika Hofbauerová:** Investigation, Writing – review & editing.

Declaration of Competing Interest

The authors declare that they have no known competing financial interests or personal relationships that could have appeared to influence the work reported in this paper.

Data availability

Data will be made available on request.

Acknowledgments

The authors acknowledge the ELETTRA Synchrotron (Trieste, Italy) for the allocation of the beamtime.

References

[1] C. Wang, P. Sahay, Breath analysis using laser spectroscopic techniques: breath biomarkers, spectral fingerprints, and detection limits, Sensors 9 (2009) 8230–8262, https://doi.org/10.3390/s91008230.

[2] A.T. Güntner, S. Abegg, K. Königstein, P.A. Gerber, A. Schmidt-Trucksäss, S. E. Pratsinis, Breath sensors for health monitoring, ACS Sens. 4 (2019) 268–280, https://doi.org/10.1021/acssensors.8b00937.

[3] M. Righettoni, A. Amann, S.E. Pratsinis, Breath analysis by nanostructured metal oxides as chemo-resistive gas sensors, Mater. Today 18 (2015) 163–171, https://doi.org/10.1016/j.mattod.2014.08.017.

[4] J. Ivanco, S. Luby, M. Jergel, P. Siffalovic, M. Benkovicova, Y. Halahovets, E. Majková, R. Rella, M.G. Manera, Nitric dioxide and acetone sensors based on iron oxide nanoparticles, Sens. Lett. 11 (2013) 2322–2326, https://doi.org/10.1166/sl.2013.3079.

[5] D.H. Kim, Y.S. Shim, J.M. Jeon, H.Y. Jeong, S.S. Park, Y.W. Kim, J.S. Kim, J.H. Lee, H.W. Jang, Vertically ordered hematite nanotube array as an ultrasensitive and rapid response acetone sensor, ACS Appl. Mater. Interfaces 6 (2014) 14779–14784, https://doi.org/10.1021/am504156w.

[6] P. Das, B. Mondal, K. Mukherjee, Facile synthesis of pseudo-peanut shaped hematite iron oxide nano-particles and their promising ethanol and formaldehyde sensing characteristics, RSC Adv. 4 (2014) 31879–31886, https://doi.org/10.1039/C4RA03098B.

[7] S. Capone, M. Benkovicova, A. Forleo, M. Jergel, M.G. Manera, P. Siffalovic, A. Taurino, E. Majkova, P. Siciliano, I. Vavra, S. Luby, R. Rella, Palladium/γ-Fe_2O_3 nanoparticle mixtures for acetone and NO_2 gas sensors, Sens. Actuators B 243 (2017) 895–903, https://doi.org/10.1016/j.snb.2016.12.027.

[8] D. Hu, B. Han, S. Deng, Z. Feng, Y. Wang, J. Popovic, M. Nuskol, Y. Wang, I. Djerdj, Novel mixed phase SnO_2 nanorods assembled with SnO_2 nanocrystals for enhancing gas-sensing performance toward isopropanol gas, J. Phys. Chem. C 118 (2014) 9832–9840, https://doi.org/10.1021/jp501550w.

[9] A. Kılıç, O. Alev, O. Özdemir, L.Ç. Arslan, S. Büyükköse, Z.Z. Öztürk, The effect of Ag loading on gas sensor properties of TiO_2 nanorods, Thin Solid Films 726 (2021), https://doi.org/10.1016/j.tsf.2021.138662, 138662-138610.

[10] D. Zhang, Z. Liu, C. Li, T. Tang, X. Liu, S. Han, B. Lei, C. Zhou, Detection of NO_2 down to ppb levels using individual and multiple In_2O_3 nanowire devices, Nano Lett. 4 (2004) 1919–1924, https://doi.org/10.1021/nl0489283.

[11] A. Shanmugasundaram, V. Gundimeda, T. Hou, D.W. Lee, Realizing synergy between In_2O_3 nanocubes and nitrogen-doped reduced graphene oxide: an excellent nanocomposite for the selective and sensitive detection of CO at ambient temperatures, ACS Appl. Mater. Interfaces 9 (2017) 31728–31740, https://doi.org/10.1021/acsami.7b06253.

[12] M. Righettoni, A. Tricoli, S.E. Pratsinis, Si:WO_3 sensors for highly selective detection of acetone for easy diagnosis of diabetes by breath analysis, Anal. Chem. 82 (2010) 3581–3587, https://doi.org/10.1021/ac902695n.

[13] M. Righettoni, A. Tricoli, S.E. Pratsinis, Thermally stable, silica-doped ε-WO_3 for sensing of acetone in the human breath, Chem. Mater. 22 (2010) 3152–3157, https://doi.org/10.1021/cm1001576.

[14] P. Gao, H. Ji, Y. Zhou, X. Li, Selective acetone gas sensors using porous WO_3–Cr_2O_3 thin films prepared by sol–gel method, Thin Solid Films 520 (2012) 3100–3106, https://doi.org/10.1016/j.tsf.2011.12.003.

[15] T. Liu, Z. Yu, Y. Liu, J. Gao, X. Wang, H. Suo, X. Yang, C. Zhao, F. Liu, Gas sensor based on Ni foam: SnO_2-decorated NiO for Toluene detection, Sens. Actuators B 318 (2020) 128167–128169, https://doi.org/10.1016/j.snb.2020.128167.

[16] A.M. Eyvaraghi, E. Mohammadi, N. Manavizadeh, E. Nadimi, L. Ma'mani, F. A. Broumand, M.A. Zeidabadi, Experimental and density functional theory computational studies on highly sensitive ethanol gas sensor based on Au-decorated ZnO nanoparticles, Thin Solid Films 741 (2022), https://doi.org/10.1016/j.tsf.2021.139014, 139014-139011.

[17] H.J. Kim, J.H. Lee, Highly sensitive and selective gas sensors using *p*-type oxide semiconductors: overview, Sens. Actuators B 192 (2014) 607–627, https://doi.org/10.1016/j.snb.2013.11.005.

[18] G. Korotcenkov, B.K. Cho, Metal oxide composites in conductometric gas sensors: achievements and challenges, Sens. Actuators B 244 (2017) 182–210, https://doi.org/10.1016/j.snb.2016.12.117.

[19] L. Zhang, W. Rong, Y. Chen, C. Lu, L. Zhao, A novel acetone sensor utilizing cataluminescence on layered double oxide, Sens. Actuators B 205 (2014) 82–87, https://doi.org/10.1016/j.snb.2014.08.064.

[20] C. Deng, J. Zhang, X. Yu, W. Zhang, X. Zhang, Determination of acetone in human breath by gas chromatography–mass spectrometry and solid-phase microextraction with on-fiber derivatization, J. Chromatogr. B 810 (2004) 269–275, https://doi.org/10.1016/j.jchromb.2004.08.013.

[21] S. Boccato, R. Torchio, S. Anzellini, E. Boulard, F. Guyot, T. Irifune, M. Harmand, I. Kantor, F. Miozzi, P. Parisiades, A.D. Rosa, D. Antonangeli, G. Morard, Melting properties by X-ray absorption spectroscopy: common signatures in binary Fe–C, Fe–O, Fe–S and Fe–Si systems, Sci. Rep. 10 (2020), https://doi.org/10.1038/s41598-020-68244-3, 11663-11613.

[22] A. Gaur, M. Stehle, M.A. Serrer, M.Z. Stummann, C.La Fontaine, V. Briois, J. D. Grunwaldt, M. Høj, Using transient XAS to detect minute levels of reversible S-O Exchange at the active sites of MoS_2-based hydrotreating catalysts: effect of metal loading, promotion, temperature, and oxygenate reactant, ACS Catal. 12 (2022) 633–647, https://doi.org/10.1021/acscatal.1c04767.

[23] M. Benkovicova, A. Holos, P. Nadazdy, Y. Halahovets, M. Kotlar, J. Kollar, P. Siffalovic, M. Jergel, E. Majkova, J. Mosnacek, J. Ivanco, Tailoring the interparticle distance in Langmuir nanoparticle films, Phys. Chem. Chem. Phys. 21 (2019) 9553–9563, https://doi.org/10.1039/C9CP02064K.

[24] L. Chitu, P. Siffalovic, E. Majkova, M. Jergel, S. Luby, Method of preparation of nanoparticle monolayers and multilayers, industrial property office of slovak republic, Patent No. 288234 (2014).

[25] L. Chitu, P. Siffalovic, E. Majkova, M. Jergel, K. Vegso, S. Luby, I. Capek, A. Satka, J. Perlich, A. Timmann, S.V. Roth, J. Keckes, G.A. Maier, Modified Langmuir-Blodgett deposition of nanoparticles – measurement of 2D to 3D ordered arrays, Meas. Sci. Rev. 10 (2010) 162–165, https://doi.org/10.2478/v10048-010-0028-0.

[26] Š. Luby, P. Siffalovic, M. Benkovicova, E. Majkova, M. Jergel, J. Ivanco, R. Rella, M.G. Manera, Gas sensing properties and electrical resistance of Langmuir-Blodgett iron oxide nanoparticle arrays, in: Proceedings of the 9th International Conference on Advanced Semiconductor Devices & Microsystems (ASDAM), Smolenice, Slovakia, 2012, pp. 175–178, https://doi.org/10.1109/ASDAM.2012.6418574.

[27] A. Di Cicco, G. Aquilanti, M. Minicucci, E. Principi, N. Novello, A. Cognigni, L. Olivi, Novel XAFS capabilities at ELETTRA synchrotron light source, J. Phys. Conf. Ser. 190 (2009) 012043–012046, https://doi.org/10.1088/1742-6596/190/1/012043.

[28] B. Ravel, M. Newville, ATHENA, ARTEMIS, HEPHAESTUS: data analysis for X-ray absorption spectroscopy using IFEFFIT, J. Synchrotron Rad. 12 (2005) 537–541, https://doi.org/10.1107/s0909049505012719.

[29] A. Gaur, B.D. Shrivastava, Speciation using X-ray absorption fine structure (XAFS), Rev. J. Chem. 5 (2015) 361–398, https://doi.org/10.1134/S2079978015040032.

[30] L. Péter, J. Osán, S. Kugler, V. Groma, S. Pollastri, A. Nagy, Comprehensive analysis of two H13-type starting materials used for laser cladding and aerosol particles formed in this process, Materials 15 (2022), https://doi.org/10.3390/ma15207367 (Basel)7367-7324.

[31] M. Wilke, F. Farges, P.E. Petit, G.E. Brown, F. Martin, Oxidation state and coordination of Fe in minerals: an Fe K-XANES spectroscopic study, Am. Mineral. 86 (2001) 714–730, https://doi.org/10.2138/am-2001-5-612.

[32] S. Pollastri, F. D'Acapito, A. Trapananti, I. Colantoni, G.B. Andreozzi, A. F. Gualtieri, The chemical environment of iron in mineral fibres. A combined X-ray absorption and Mössbauer spectroscopic study, J. Hazard. Mater. 298 (2015) 282–293, https://doi.org/10.1016/j.jhazmat.2015.05.010.

[33] A. Espinosa, A. Serrano, A. Llavona, J. Jimenez de la Morena, M. Abuin, A. Figuerola, T. Pellegrino, J.F. Fernández, M. Garcia-Hernandez, G.R. Castro, M. A. Garcia, On the discrimination between magnetite and maghemite by XANES measurements in fluorescence mode, Meas. Sci. Technol. 23 (2012) 015602–015606, https://doi.org/10.1088/0957-0233/23/1/015602.

[34] C. Piquer, M. Laguna-Marco, A.G. Roca, R. Boada, C. Guglieri, J. Chaboy, Fe K-edge X-ray absorption spectroscopy study of nanosized nominal magnetite, J. Phys. Chem. C 118 (2014) 1332–1346, https://doi.org/10.1021/jp4104992.

[35] S. Bajt, S.R. Sutton, J.S. Delaney, X-ray microprobe analysis of iron oxidation states in silicates and oxides using X-ray absorption near edge structure (XANES), Geochim. Cosmochim. Acta 58 (1994) 5209–5214, https://doi.org/10.1016/0016-7037(94)90305-0.

[36] E. Pellegrin, M. Hagelstein, S. Doyle, H.O. Moser, J. Fuchs, D. Vollath, S. Schuppler, M.A. James, S.S. Saxena, L. Niesen, O. Rogojanu, G.A. Sawatzky, C. Ferrero, M. Borowski, O. Tjernberg, N.B. Brookes, Characterization of nanocrystalline γ-Fe_2O_3 with synchrotron radiation techniques, phys. Stat. Sol. 215 (1999) 797–801, https://doi.org/10.1002/(SICI)1521-3951(199909)215:1<797::AID−PSSB797>3.0.CO;2-D.

[37] A. Corrias, G. Ennas, G. Mountjoy, G. Paschina, An X-ray absorption spectroscopy study of the Fe K edge in nanosized maghemite and in Fe_2O_3–SiO_2 nanocomposites, Phys. Chem. Chem. Phys. 2 (2000) 1045–1050, https://doi.org/10.1039/A908698F.

[38] R. Nemausat, C. Gervais, C. Brouder, N. Trcera, A. Bordage, C. Coelho-Diogo, P. Florian, A. Rakhmatullin, I. Errea, L. Paulatto, M. Lazzeri, D. Cabaret, Temperature dependence of X-ray absorption and nuclear magnetic resonance spectra: probing quantum vibrations of light elements in oxides, Phys. Chem. Chem. Phys. 19 (2017) 6246–6256, https://doi.org/10.1039/C6CP08393E.

[39] G. Ketteler, W. Weiss, W. Ranke, R. Schlögl, Bulk and surface phases of iron oxides in an oxygen and water atmosphere at low pressure, Phys. Chem. Chem. Phys. 3 (2001) 1114–1122, https://doi.org/10.1039/B009288F.

[40] F. Genuzio, A. Sala, T. Schmidt, D. Menzel, H.J. Freund, Interconversion of α-Fe_2O_3 and Fe_3O_4 thin films: mechanisms, morphology, and evidence for unexpected substrate participation, J. Phys. Chem. C 118 (2014) 29068–29076, https://doi.org/10.1021/jp504020a.

[41] C. Schlueter, M. Lübbe, A.M. Gigler, W. Moritz, Growth of iron oxides on Ag(111) — reversible Fe_2O_3/Fe_3O_4 transformation, Surf. Sci. 605 (2011) 1986–1993, https://doi.org/10.1016/j.susc.2011.07.019.

[42] B.J. Evans, Experimental studies of the electrical conductivity and phase transition in Fe_3O_4, AIP Conf. Proc. 24 (1975) 73–78, https://doi.org/10.1063/1.30264.

[43] N.N. Greenwood, A. Earnshaw, 25 - iron, ruthenium and osmium. Chemistry of the Elements, Butterworth-Heinemann, Oxford, 1997, pp. 1070–1112.

[44] G. Busca, V. Lorenzelli, Infrared study of the reactivity of acetone and hexachloroacetone adsorbed on haematite, J. Chem. Soc. Faraday Trans. 78 (1982) 2911–2919, https://doi.org/10.1039/F19827802911, 1.

[45] J.M. Vohs, M.A. Barteau, Structure sensitivity, selectivity, and adsorbed intermediates in the reactions of acetone and *2*-propanol on the polar surfaces of zinc oxide, J. Phys. Chem. 95 (1991) 297–302, https://doi.org/10.1021/j100154a055.

[46] K.G. Pierce, M.A. Barteau, Ketone coupling on reduced TiO_2 (001) surfaces: evidence of pinacol formation, J. Org. Chem. 60 (1995) 2405–2410, https://doi.org/10.1021/jo00113a021.

[47] R.I. King, S.D. Senanayake, S.V. Chong, H. Idriss, The reactions of acetone with the surfaces of uranium dioxide single crystal and thin film, Surf. Sci. 601 (2007) 5690–5700, https://doi.org/10.1016/j.susc.2007.06.071.

[48] S.D. Senanayake, W.O. Gordon, S.H. Overbury, D.R. Mullins, Adsorption and reaction of acetone over CeO_x(111) thin films, J. Phys. Chem. C 113 (2009) 6208–6214, https://doi.org/10.1021/jp810403d.

[49] R.H. Fowler, L. Nordheim, Electron emission in intense electric fields, Proc. R. Soc. Lond. A 119 (1928) 173–181, https://doi.org/10.1098/rspa.1928.0091.

[50] J. Frenkel, On the electrical resistance of contacts between solid conductors, Phys. Rev. 36 (1930) 1604–1618, https://doi.org/10.1103/PhysRev.36.1604.
[51] J. Herrmann, K.H. Müller, T. Reda, G.R. Baxter, B. Raguse, G.J.J.B.D. Groot, R. Chai, M. Roberts, L. Wieczorek, Nanoparticle films as sensitive strain gauges, Appl. Phys. Lett. 91 (2007), https://doi.org/10.1063/1.2805026, 183105-183103.
[52] J. Ivančo, K. Végsö, P. Šiffalovič, D. Kostiuk, Y. Halahovets, I. Klačková, M. Kotlár, Š. Luby, E. Majková, Morphological and electrical properties of stretched nanoparticle layers, Key Eng. Mater. 644 (2015) 31–34, https://doi.org/10.4028/www.scientific.net/KEM.644.31.
[53] X. Wei, T. Xie, L. Peng, W. Fu, J. Chen, Q. Gao, G. Hong, D. Wang, Effect of heterojunction on the behavior of photogenerated charges in Fe_3O_4@Fe_2O_3 nanoparticle photocatalysts, J. Phys. Chem. C 115 (2011) 8637–8642, https://doi.org/10.1021/jp111250z.